Fusion Engineering and Design 192 (2023) 113796

Contents lists available at ScienceDirect

Fusion Engineering and Design

journal homepage: www.elsevier.com/locate/fusengdes

Model predictive current profile control in tokamaks by exploiting spatially moving electron cyclotron current drives

Sai Tej Paruchuri *, Zibo Wang, Tariq Rafiq, Eugenio Schuster

Mechanical Engineering and Engineering Mechanics, Lehigh University, Bethlehem, PA, USA

ARTICLE INFO

Keywords:
Current profile control
Moving EC H&CD
Model predictive control

ABSTRACT

The plasma control systems in next-generation tokamaks like ITER will balance competing control objectives to achieve the desired level of performance in advanced scenarios while preventing magnetohydrodynamic instabilities and disruptions. During normal tokamak operation, the points of incidence of the electromagnetic waves generated by the electron cyclotron heating and current drives (EC H&CDs) are usually fixed in space. However, the points of incidence can be modified in real-time by changing the angles of the mirrors that reflect the EC H&CD waves. Altering the points of incidence, in turn, varies the ability of the plasma control system to regulate a plasma property. For instance, changing the EC H&CD wave incidence location may place the power demands necessary to achieve a particular plasma target within saturation limits. Therefore, using the EC H&CD deposition location, which is related to the EC H&CD mirror angle, as a supplementary controllable variable may facilitate access to a given target scenario. However, active scenario-control algorithms have not been designed so far to fully exploit this capability in real time. In this work, a model predictive controller that can handle actuation locations as control inputs is developed. In particular, the controller is designed to regulate both the auxiliary powers and the EC H&CD deposition locations in a pre-defined optimal sense to achieve the control objective of attaining and sustaining a target current profile. The proposed controller is tested for a DIII-D tokamak scenario in nonlinear simulations using the Control Oriented Transport SIMulator (COTSIM).

1. Introduction

Maintaining the toroidal current density profile at preset levels is critical in achieving advanced scenarios associated with high bootstrap current fraction and steady-state operation. In addition, deviation of the current profile from preset levels can result in the emergence of magnetohydrodynamic (MHD) instabilities that can disrupt the confined plasma. Control strategies that can actively shape the current density profile to achieve the desired target have been developed over the past decade. Examples of existing solutions include linear quadratic optimal control [1–4], model predictive control [5–7], robust control [4,8], infinite-dimensional control [9–11], passivity-based control [12], backstepping control [13], H_∞ control [14], feedback linearization [15,16]. In general, the above cited control strategies determine in real time the auxiliary heating and current drive (H&CD) powers and/or plasma current to shape the current profile during the plasma discharge.

The number of H&CD actuators available for current profile regulation and their corresponding saturation bounds define the feasible set of target current profiles that can be achieved in any given scenario. However, next-generation tokamaks like ITER and DEMO must handle multiple control objectives simultaneously, and the plasma control algorithms in these tokamaks must share the available auxiliary drives to achieve the desired targets. As a result, the H&CD actuation capability for current profile regulation is limited not only by the number of H&CD sources and their saturation bounds but also by their functionalities. Thus, it is highly desirable to develop strategies that can increase the feasible set of the target current profiles and enable better profile shaping in a given scenario.

One potential solution to increase the current profile shaping capabilities of the tokamak with a limited actuation capability is to use moving actuators. Here, the controllers determine the auxiliary powers and moving positions of the actuators in real time to achieve the desired target profile [17]. The additional degrees of freedom provided by the moving actuator positions can potentially make previously unfeasible profiles now feasible. A control strategy involving moving actuators clearly requires the availability of specific auxiliary H&CD sources whose deposition positions can be updated in real-time. Electron cyclotron heating and current drives (EC H&CDs) generate electromagnetic waves with frequencies equal to that of the electron

* Corresponding author.
E-mail address: saitejp@lehigh.edu (S.T. Paruchuri).

https://doi.org/10.1016/j.fusengdes.2023.113796
Received 31 October 2022; Received in revised form 14 April 2023; Accepted 2 May 2023
Available online 19 May 2023

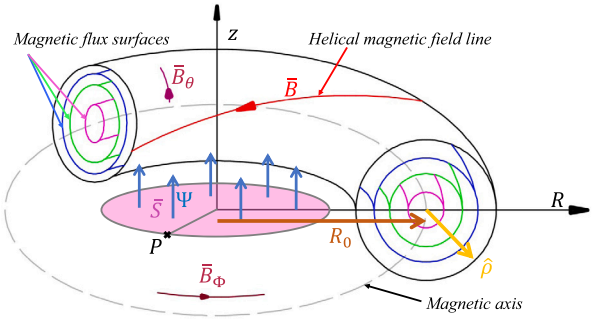

Fig. 1. Tokamak magnetic field lines and flux surfaces illustration.

cyclotron frequency. The resulting electron resonance can be used to heat the plasma and drive current. Importantly, reflecting mirrors can be used to control the point of incidence of EC H&CD waves. Since the angle of the reflecting mirrors can be updated in real-time, a moving actuator strategy can be implemented when EC H&CDs are available for current profile control.

Profile control with moving H&CD sources is a relatively unexplored area of research. A feedback-linearization-based control algorithm has been proposed in [17] to regulate spatially-moving local properties of the safety factor profile, such as its minimum value, by using spatially-moving EC H&CD sources. In this work, a control algorithm based on model predictive control (MPC) is developed to allocate auxiliary powers and the EC H&CD deposition locations (the points of incidence of the waves generated by EC H&CDs) to achieve the desired target current profile. The advantage of such an algorithm is that it can be adapted to other profile control problems where varying EC H&CD current depositions can be advantageous. Furthermore, algorithms based on MPC allow easy incorporation of state and actuator constraints and can be tuned to produce smooth inputs.

This paper is organized as follows. Section 2 derives the linearized-control-oriented model based on the magnetic diffusion equation. Section 3 formulates the MPC algorithm for safety-factor control with moving EC H&CD sources. The results of numerical simulations are presented in Section 4. The conclusions of this work and potential future extensions are discussed in Section 5.

2. Control model derivation

The flux Ψ produced by the poloidal magnetic field $\bar{B}_\theta$ at any given location P in the tokamak is given by $\Psi := \int_S \bar{B}_\theta \cdot d\bar{S}$. Here, the term S represents the surface enclosed by the loop passing through the point P as shown in Fig. 1. Under ideal MHD conditions, regions with equal magnetic flux, commonly referred to as flux surfaces, form a series of nested surfaces (Fig. 1). Critical plasma properties like the toroidal current density, safety factor and plasma pressure are equal on these flux surfaces. Thus, any parameter that indexes the flux surfaces can be used as the spatial variable while modeling the dynamics of critical plasma properties like the current profile. In this work, the normalized mean effective minor radius, defined as

$$\hat{\rho} := \frac{\rho}{\rho_b} \tag{1}$$

is used as the indexing parameter. Here, the term ρ is the mean effective minor radius and is given by

$$\rho := \sqrt{\frac{\Phi}{B_{\phi,0}\pi}}, \tag{2}$$

where Φ and $B_{\phi,0}$ are the toroidal magnetic flux and the (magnitude of the) toroidal magnetic field at the major radius R_0, respectively. The term $\hat{\rho}$ is computed by normalizing ρ with respect to mean effective minor radius at the last closed flux surface ρ_b.

The toroidal current density at location $\hat{\rho}$ and time t is defined as

$$j_\phi(\hat{\rho},t) := -\frac{1}{\mu_0 \rho_b^2 R_0 \hat{H}} \frac{1}{\hat{\rho}} \frac{\partial}{\partial \hat{\rho}} \left[\hat{\rho} \hat{G} \hat{H} \frac{\partial \psi}{\partial \hat{\rho}} \right], \tag{3}$$

where $\psi := \Psi/2\pi$ is the poloidal stream function, μ_0 is the vacuum permeability, $\hat{G}$, $\hat{H}$ are the geometric factors that define the plasma equilibrium. The safety factor, a plasma parameter that characterizes the pitch of the helical magnetic field and is critical to MHD stability, is defined as

$$q(\hat{\rho},t) := -\frac{d\Phi}{d\Psi} = -\frac{\partial\Phi/\partial\hat{\rho}}{\partial\Psi/\partial\hat{\rho}} = -\frac{B_{\phi,0}\rho_b^2\hat{\rho}}{\partial\psi/\partial\hat{\rho}}. \tag{4}$$

From (3) and (4), it is clear that the toroidal current density j_ϕ, the safety factor q and the poloidal flux gradient $\theta := \partial\psi/\partial\hat{\rho}$ are related to each other. Thus, the regulation of one of these properties can be reformulated as the regulation of any of the other two. The model for control design used in this work is derived from the magnetic diffusion equation (MDE), which is a partial differential equation (PDE) that governs the evolution of ψ [18]. To simplify the MDE, $0.5D$ control-oriented models for the plasma resistivity η, non-inductive current j_{ni}, electron density n_e and electron temperature T_e are used [19]. These $0.5D$ equations model the evolution of n_e and T_e by using empirical laws. Closing the MDE with the control-oriented models results in a PDE of the form

$$\frac{\partial\psi}{\partial t} = \left(f_1\psi' + f_2\psi''\right)u_\eta + \sum_{i=1}^{n_{nb}} f_{nb,i}u_{nb,i} + \sum_{j=1}^{n_{ec}} f_{ec,j}u_{ec,j} + \frac{f_{bs}}{\psi'}u_{bs}, \tag{5}$$

subject to the boundary conditions

$$\psi'|_{\hat{\rho}=0} = 0, \quad \psi'|_{\hat{\rho}=1} = -k_{I_p} I_p. \tag{6}$$

The above control-oriented model was first introduced in [19] and successfully implemented in [16,17,20]. In the above model, the notation $(\cdot)'$ represents the derivative with respect to the spatial variable $\hat{\rho}$. In (5), the terms f_1 and f_2 model the spatial distribution of the flux diffusion, f_{nb} and f_{ec} model the spatial effect of NBIs and EC H&CDs, respectively, f_{bs} models the spatial distribution of the bootstrap current, and k_{I_p} models the effect of the plasma current I_p on the boundary. The terms u_η, $u_{nbi,i}$, $u_{ec,j}$, u_{bs} are virtual inputs corresponding to the flux diffusion, ith NBI, jth EC H&CD and the bootstrap current, respectively. The assumption is that there are n_{nb} NBIs and n_{ec} EC H&CDs available for current profile control, and hence $i \in \{1,\dots,n_{nb}\}$ and $j \in \{1,\dots,n_{ec}\}$. The virtual inputs are defined as

$$u_\eta := (I_p^\gamma P_{tot}^\epsilon \bar{n}_e^\zeta)^{-3/2}, \tag{7}$$

$$u_{nbi,i} := (I_p^\gamma P_{tot}^\epsilon \bar{n}_e^\zeta)^{(-3/2+\zeta_{nb})} \bar{n}_e^{-1} P_{nb,i}, \tag{8}$$

$$u_{ec,j} := (I_p^\gamma P_{tot}^\epsilon \bar{n}_e^\zeta)^{(-3/2+\zeta_{ec})} \bar{n}_e^{-1} P_{ec,j}, \tag{9}$$

$$u_{bs} := (I_p^\gamma P_{tot}^\epsilon \bar{n}_e^\zeta)^{-1/2} \bar{n}_e \tag{10}$$

where P_{tot} and $\bar{n}_e$ are the total power and line-averaged electron density, respectively. The terms γ, ϵ, ζ, ζ_{nb}, ζ_{ec} are constants introduced by scaling laws. Finally, the variables $P_{nb,i}$ and $P_{ec,j}$ represent the ith NBI power and jth EC H&CD power, respectively. Note that the total power is related to the NBI and EC H&CD powers as

$$P_{tot} = P_{ohm} - P_{rad} + \sum_{i=1}^{n_{nb}} P_{nb} + \sum_{j=1}^{n_{ec}} P_{ec}, \tag{11}$$

where P_{ohm} and P_{rad} are the ohmic and radiated power, respectively. The ohmic and radiated power are calculated using the equations

$$P_{ohm} = C_{ohm}u_{ohm}, \tag{12}$$

$$P_{rad} = C_{rad}u_{rad}, \tag{13}$$

where C_{ohm} and C_{rad} are constants that account for the global plasma resistance and global radiation losses [21]. On the other hand, u_{ohm} and u_{rad} are virtual input terms and are defined as

$$u_{ohm} := I_p^{2-1.5\gamma} P_{tot}^{-1.5\epsilon} \bar{n}_e^{-1.5\zeta}, \tag{14}$$

$$u_{rad} := I_p^{0.5\gamma} P_{tot}^{0.5\epsilon} \bar{n}_e^{2+0.5\zeta}. \tag{15}$$

In the above model, the effect of spatially moving EC H&CD sources on the ψ dynamics was not considered. Particularly, the function $f_{ec,j}$ corresponds to a default EC H&CD deposition location $\rho_{ec,j}$. The relation between the two parameters can be explicitly seen from the equation

$$f_{ec,j}(\hat{\rho}) = \underbrace{R_0 \hat{H}(\hat{\rho}) \frac{(T_e^{prof}(\hat{\rho})(n_e^{prof}(\hat{\rho}))^{\zeta})^{\lambda_{EC}}}{n_e^{prof}(\hat{\rho})}}_{g_{ec}(\hat{\rho})} j_{ec,j}^{prof}, \tag{16}$$

where T_e^{prof} and n_e^{prof} are fixed functions of $\hat{\rho}$ arising from the control-oriented models for T_e and n_e, respectively, and λ_{EC} is a constant that accounts for the efficiency of the EC H&CDs. The term $j_{ec,j}^{prof}$ is the current deposition profile of the jth EC H&CD that is located at $\rho_{ec,j}$. To incorporate the EC H&CD moving-deposition-location dynamics, a shifting current deposition model, first introduced in [17], is used. Suppose the EC H&CD deposition location varies from $\rho_{ec,j}$ to $\bar{\rho}_{ec,j}$. The new current deposition profile $\bar{j}_{ec,j}^{prof}$ is given by

$$\bar{j}_{ec,j}^{prof}(\rho_{ec,j}, \hat{\rho}) := j_{ec,j}^{prof}(\hat{\rho} + \bar{\rho}_{ec,j} - \rho_{ec,j}). \tag{17}$$

Incorporating the new shifting current deposition profile into (16) results in a new function $\bar{f}_{ec,j}$ that depends on both the spatial variable $\hat{\rho}$ and the EC H&CD deposition location $\rho_{ec,j}$. Replacing $f_{ec,j}$ with $\bar{f}_{ec,j}$ in the MDE (5) and taking the derivative with respect to spatial variable $\bar{\rho}$ results in a partial differential equation (PDE) of the form

$$\begin{aligned}\frac{\partial \theta}{\partial t} &= \left(h_{\eta,1}\theta'' + h_{\eta,2}\theta' + h_{\eta,3}\theta\right) u_\eta + \sum_{i=1}^{n_{nb}} h_{nb,i} P_{nb,i} \\ &+ \sum_{j=1}^{n_{ec}} h_{ec,j}(\rho_{ec,j}) P_{ec,j} + \left(\frac{h_{bs,1}}{\theta} - h_{bs,2}\frac{\theta'}{\theta^2}\right) u_{bs},\end{aligned} \tag{18}$$

where the fixed spatial profiles are given by $h_{\eta,1} = f_2$, $h_{\eta,2} = f_1 + f_2'$, $h_{\eta,3} = f_1'$, $h_{bs,1} = f_{bs}'$, $h_{bs,2} = f_{bs}$. The terms $h_{nb,i}$, $h_{ec,j}(\rho_{ec,j})$, on the other hand, are functions of the spatial variable $\hat{\rho}$ and time t, and they are given by

$$h_{nb,i} = f_{nb,i}' \times (I_p^\gamma P_{tot}^\epsilon \bar{n}_e^\zeta)^{(-3/2+\zeta_{nb})} \bar{n}_e^{-1}, \tag{19}$$

$$h_{ec,j}(\rho_{ec,j}) = \bar{f}_{ec,j}'(\rho_{ec,j}, \cdot) \times (I_p^\gamma P_{tot}^\epsilon \bar{n}_e^\zeta)^{(-3/2+\zeta_{ec})} \bar{n}_e^{-1}. \tag{20}$$

Since the EC H&CD deposition locations are allowed to vary, the terms $\rho_{ec,j}$ in (18) are functions of time t. The Neumann boundary conditions given in (6) become Dirichlet boundary conditions of the form

$$\theta(0,t) = 0, \qquad \theta(1,t) = -k_{I_p} I_p. \tag{21}$$

To simplify the governing equation, a finite difference scheme is implemented. An uniform grid of $N+1$ spatial nodes at $\hat{\rho}_0, \ldots, \hat{\rho}_N$ and $M+1$ temporal nodes at $t_0, \ldots, t_M$ are considered in the spatial domain $[0,1]$ and time domain $[t_0, t_{end}]$, respectively. Evaluating the PDE (18) at the interior nodes ($\hat{\rho}_1, \ldots, \hat{\rho}_{N-1}$ and $t_1, \ldots, t_{M-1}$) and using the central finite difference approximations for first and second order derivatives results in a difference equation of the form

$$\boldsymbol{z}_{k+1} = f(k, \boldsymbol{z}_k, \boldsymbol{u}_k, \boldsymbol{\rho}_{ec,k}), \tag{22}$$

where

$$\boldsymbol{z}_k = [\theta(\hat{\rho}_1, t_k), \ldots, \theta(\hat{\rho}_{N-1}, t_k)]^T, \tag{23}$$

$$\boldsymbol{u}_k = [\boldsymbol{P}_{nb}(t_k)^T, \boldsymbol{P}_{ec}(t_k)^T, I_p(t_k)]^T, \tag{24}$$

$$\boldsymbol{P}_{nb}(t_k) = [P_{nb,1}(t_k), \ldots, P_{nb,n_{nb}}(t_k)]^T, \tag{25}$$

$$\boldsymbol{P}_{ec}(t_k) = [P_{ec,1}(t_k), \ldots, P_{ec,n_{ec}}(t_k)]^T, \tag{26}$$

$$\boldsymbol{\rho}_{ec,k} = [\rho_{ec,1}(t_k), \ldots, \rho_{ec,n_{ec}}(t_k)]^T. \tag{27}$$

The above model is further simplified by fixing the EC H&CD deposition locations at $\bar{\rho}_{ec}$ and linearizing the nonlinear function f around a reference trajectory $(\boldsymbol{z}_{ref}, \boldsymbol{u}_{ref})$. The resulting linear equation has the form

$$\delta \boldsymbol{z}_{k+1} = A_k \delta \boldsymbol{z}_k + B_{k,\bar{\rho}_{ec}} \delta \boldsymbol{u}_k, \tag{28}$$

where $\delta \boldsymbol{z}_k = \boldsymbol{z}_k - \boldsymbol{z}_{ref,k}$, $\delta \boldsymbol{u}_k = \boldsymbol{u}_k - \boldsymbol{u}_{ref,k}$,

$$A_k = \left.\frac{\partial f}{\partial \boldsymbol{z}_k}\right|_{(\boldsymbol{z}_{ref,k}, \boldsymbol{u}_{ref,k})}, \quad B_{k,\bar{\rho}_{ec}} = \left.\frac{\partial f}{\partial \boldsymbol{u}_k}\right|_{(\boldsymbol{z}_{ref,k}, \boldsymbol{u}_{ref,k})}. \tag{29}$$

The above linear equation is imposed as a linear constraint in the MPC problem formulation. Note that the above linear equation assumes that the EC H&CD deposition location is fixed at $\bar{\rho}_{ec}$. This assumption simplifies the model derivation and MPC problem formulation. The EC H&CD deposition locations are updated by the controller using an iterative approach as discussed in Section 3. The controller must also account for the constraint on total power that is given by (11). This constraint can be written as a nonlinear equation of the form

$$P_{tot,k} = g\left(k, \boldsymbol{u}_k, P_{tot,k}\right), \tag{30}$$

where $P_{tot,k} = P_{tot}(t_k)$. For easier MPC implementation, this nonlinear equation is also linearized around a reference trajectory $(\boldsymbol{u}_{ref}, P_{tot,ref})$. The resulting linear equation has the form

$$r_k \delta P_{tot,k} + \boldsymbol{s}_k^T \delta \boldsymbol{u}_k = 0 \tag{31}$$

with $r_k \in \mathbb{R}$, $\boldsymbol{s}_k \in \mathbb{R}^{n_{nb}+n_{ec}+1}$, $\delta P_{tot,k} = P_{tot,k} - P_{tot,k,ref}$.

3. Control problem-formulation and design

The model predictive controller solves a finite horizon optimal control problem (FHOCP) at each time step. Traditional MPC algorithms may not achieve perfect tracking in the presence of plant/model mismatch. To overcome this limitation, the MPC problem is formulated in velocity form [22] in this work, i.e., the cost function and constraints are defined in terms of state and input increments.

The variations of the EC H&CD deposition locations also introduce another layer of complexity into the MPC problem. To simplify the problem, the MPC problem is first formulated for fixed EC H&CD deposition locations based on the linear model (28). Then an iterative algorithm is wrapped around the MPC algorithm to compute the optimal EC H&CD deposition locations at each time step. Suppose a target $\boldsymbol{z}_{tar,k}$ is given. Define $\delta \boldsymbol{z}_{tar,k} := \boldsymbol{z}_{tar,k} - \boldsymbol{z}_{ref,k}$. The MPC problem is formulated as follows: at any given time step t_k,

$$\min_{U_k \in \mathcal{U}_k} \sum_{j=k}^{k+L} (\delta \boldsymbol{z}_j - \delta \boldsymbol{z}_{tar,j})^T Q (\delta \boldsymbol{z}_j - \delta \boldsymbol{z}_{tar,j}) + \delta \boldsymbol{u}_j^T R \delta \boldsymbol{u}_j$$

such that (28) and (31) hold. In the above formulation, L represents the horizon length over which the FHOCP is solved, U_k is the input trajectory matrix defined as $U_k := \left[\delta \boldsymbol{u}_k, \ldots \delta \boldsymbol{u}_{k+L}\right]^T$, $\mathcal{U}_k$ is set of feasible input trajectories. The set $\mathcal{U}_k$ incorporates only the inputs that are within the physical bounds (such as saturation limits and rates) of the actuators. To formulate the same problem in the velocity form, the increment terms are defined as

$$\Delta \boldsymbol{z}_k := \delta \boldsymbol{z}_k - \delta \boldsymbol{z}_{k-1}, \tag{32}$$

$$\Delta \boldsymbol{z}_{tar,k} := \delta \boldsymbol{z}_{tar,k} - \delta \boldsymbol{z}_{tar,k-1}, \tag{33}$$

$$\Delta \boldsymbol{u}_k := \delta \boldsymbol{u}_k - \delta \boldsymbol{u}_{k-1}, \tag{34}$$

$$\Delta U_k := U_k - U_{k-1}, \tag{35}$$

$$\Delta P_{tot,k} := \delta P_{tot,k} - \delta P_{tot,k-1}. \tag{36}$$

Furthermore, the difference in the linearized model terms between any two consecutive time steps, namely A_{k-1}, B_{k-1}, r_{k-1}, and s_{k-1} at time t_{k-1} and A_k, B_k, r_k, and s_k at time t_k, respectively, is assumed

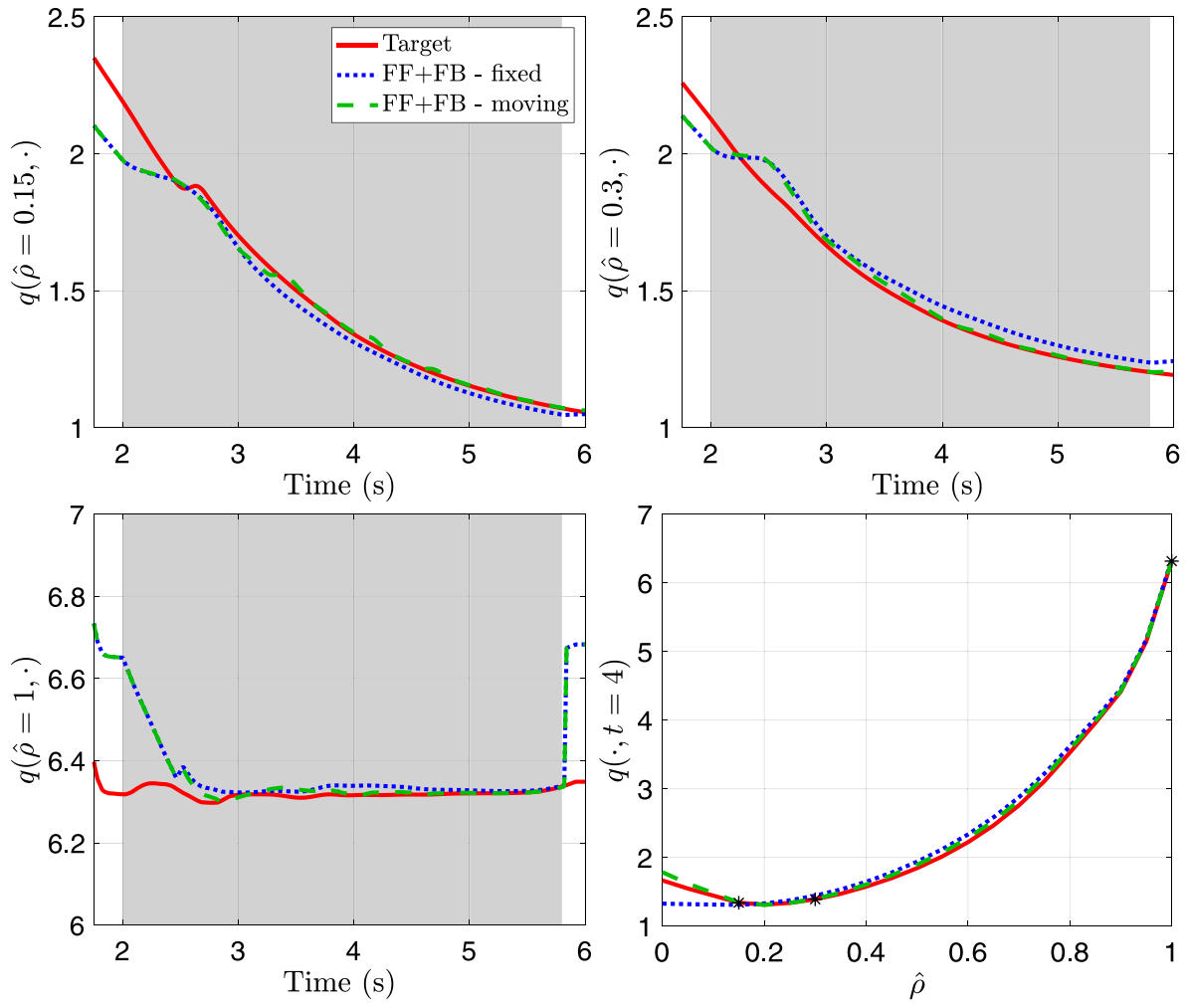

Fig. 2. Safety factor comparisons of fixed and varying EC H&CD deposition locations cases — top right: $q(\hat{\rho} = 0.15, \cdot)$, top left: $q(\hat{\rho} = 0.3, \cdot)$, bottom right: $q(\hat{\rho} = 1, \cdot)$, bottom left: $q(\cdot, t = 4)$.

to be negligible. The velocity form of the MPC problem can now be formulated as follows: at each time step t_k,

$$\min_{\Delta U_k \in \Delta \mathcal{U}_k} \sum_{j=k}^{k+L} (\Delta \boldsymbol{z}_j - \Delta \boldsymbol{z}_{tar,j})^T Q (\Delta \boldsymbol{z}_j - \Delta \boldsymbol{z}_{tar,j}) + \Delta \boldsymbol{u}_j^T R \Delta \boldsymbol{u}_j,$$

such that

$$\Delta \boldsymbol{z}_{i+1} = A_i \Delta \boldsymbol{z}_i + B_{i,\bar{\rho}_{ec}} \Delta \boldsymbol{u}_i, \tag{37}$$

$$r_i \Delta P_{tot,i} + \boldsymbol{s}_i^T \Delta \boldsymbol{u}_i = 0 \tag{38}$$

hold for $i = k, \ldots, k + L - 1$. Note that the set $\Delta \mathcal{U}_k$ now consists of feasible input increments rather than feasible input trajectories. This MPC problem can be solved using quadratic programming algorithms like sequential quadratic programming and active-set methods [23].

To incorporate the EC H&CD deposition locations' variation into the control algorithm, the above MPC problem is solved multiple times with varying EC H&CD deposition location combinations. Suppose the EC H&CD deposition locations at time step $k - 1$ are given by $\rho_{ec,1}, \ldots, \rho_{ec,n_{ec}}$. Let Ω be the set of possible positions that EC H&CDs can take at the next time step. For instance, if there are 2 EC H&CDs both at $\check{\rho}_{ec}$ and if the EC H&CDs can take 3 positions at the next time step (say $\check{\rho}_{ec} - \delta, \check{\rho}_{ec}, \check{\rho}_{ec} + \delta$ for some constant δ), then the set Ω consists of 9 possible combinations of the EC H&CD deposition locations. Note that the MPC problems corresponding to different EC H&CD deposition location combinations differ only in the value of $B_{\bar{\rho}_{ec}}$. To determine the optimal EC H&CD deposition location, the MPC problem corresponding to each element in Ω (each combination of potential EC H&CD deposition locations) is solved and the EC H&CD deposition locations and inputs corresponding to the least cost function value are selected. Note that the assumption is that the EC H&CD deposition locations across the horizon length of the MPC problem are fixed. The proposed algorithm provides a straightforward method for incorporating EC positions as a controllable variable into existing MPC algorithms. Furthermore, by selecting a feasible set of EC positions Ω at each time step, the proposed method inherently accounts for constraints on the rate of change of EC mirror angles. In addition, since the MPC problems corresponding to different elements of the set Ω are independent, the algorithm allows for implementing parallel computing techniques to reduce computation time. Alternative approaches can rely on incorporating EC positions as controllable variables and optimizing both the EC powers and the EC positions simultaneously. However, treating EC positions as continuous variables would demand the incorporation of the mirror angle bounds and rate-of-change limits into the problem. On the other hand, if EC deposition locations are treated as discrete variables, such as in this work, simultaneous EC power and position optimization would require the implementation of a hybrid MPC. Furthermore, it might not be possible to exploit parallel computing in a simultaneous optimization approach since the deposition locations are coupled with the dynamics. Despite the above-mentioned points, simultaneous optimization might be more computationally efficient than the proposed algorithm in scenarios with many EC H&CDs.

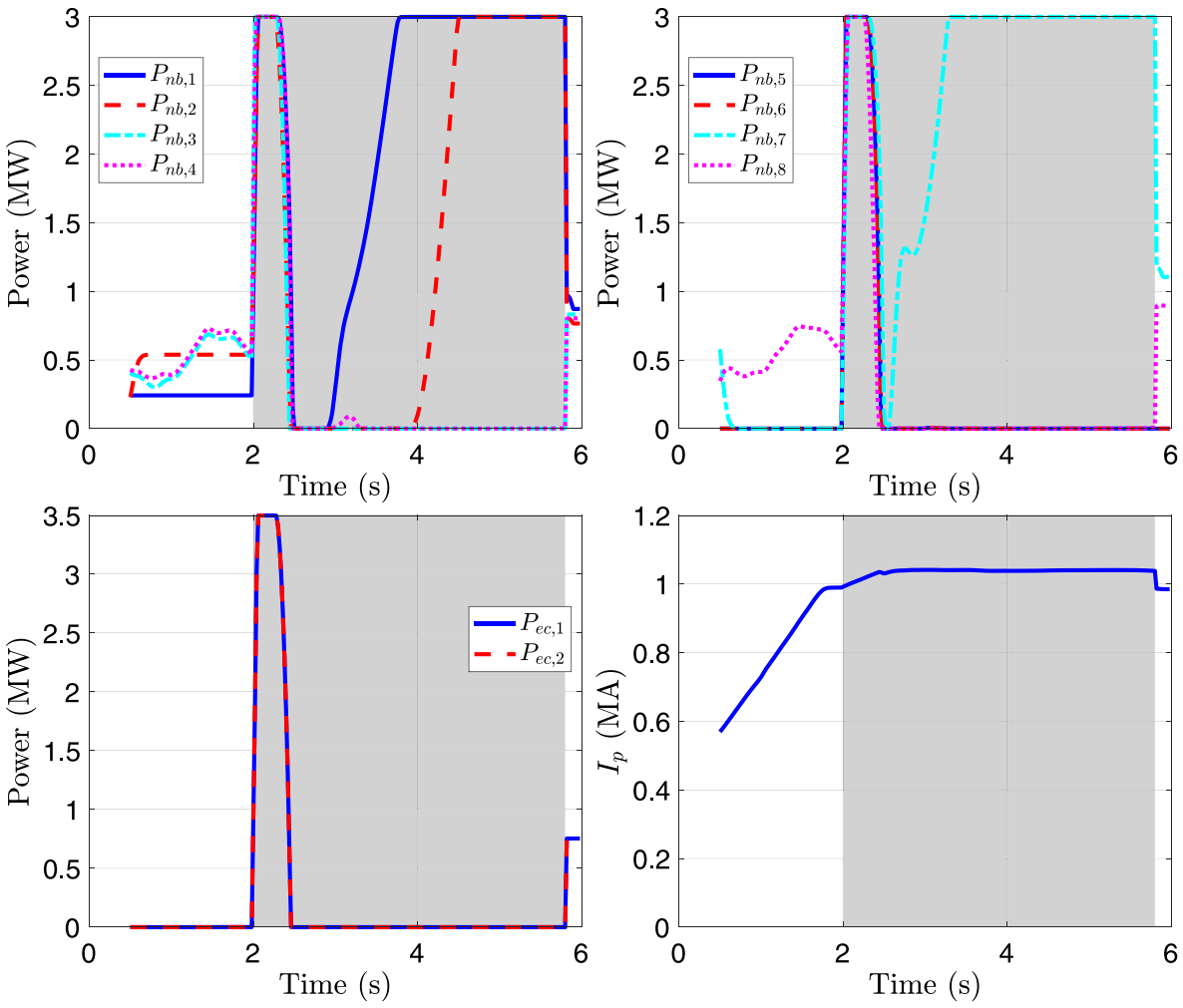

Fig. 3. Inputs of fixed EC H&CD deposition locations case — top right: $P_{nb,i}, i \in \{1,2,3,4\}$, top left: $P_{nb,i}, i \in \{5,6,7,8\}$, bottom right: $P_{ec,i}, i \in \{1,2\}$, bottom left: I_p.

4. Performance assessment via nonlinear numerical simulations

The proposed control algorithm was tested for a DIII-D tokamak scenario in the Control-Oriented Transport Simulator (COTSIM) [24]. The simulator used the 1D magnetic diffusion equation and the heat transport equation based on the Bohm/Gyro-Bohm transport model to simulate the plasma dynamics. The DIII-D configuration of shot 147634 was used in the simulations. A total of 8 NBIs and 2 EC H&CD clusters were utilized during the simulations. Of the 8 NBIs, NBI_1, NBI_2, NBI_7, NBI_8 were on-axis co-current NBIs, NBI_3, NBI_4 were off-axis co-current NBIs, and NBI_5, NBI_6 were counter-current NBIs. The saturation limits of the NBIs and EC H&CDs were 3 MW and 3.5 MW, respectively. The horizon length of the MPC was selected as 3 time steps. The safety factor values at three locations ($\hat{\rho} = 0.15, 0.3, 1$) were regulated by the controller. The controller was active between 2 and 5.8 s. Two different test cases were simulated. In the first case, the EC H&CD deposition locations were assumed to be fixed at $\hat{\rho} = 0.5$. This test case was considered to contrast the simulation results with the second case, where the EC H&CD deposition locations were allowed to vary when the controller was active. In the second case, the ith EC H&CD was allowed to take one of the three possible positions $\rho_{ec,k-1,i} - 0.01$, $\rho_{ec,k-1,i}$, $\rho_{ec,k-1,i} + 0.01$ at each time step, where $\rho_{ec,k-1,i}$ is the ith EC H&CD deposition location at the previous time-step ($i = 1, 2$). In the simulations, the time-step increments were fixed at 0.02 s, i.e., $t_k - t_{k-1} = 0.02$ s.

Fig. 2 shows the safety factor values achieved during the closed-loop (feedforward + feedback) simulations of the two test cases. The figure indicates that the controller was not able to achieve the desired target in the first case. The controller drives the closed-loop trajectory towards the target at $\hat{\rho} = 0.15, 0.3, 1$. However, perfect tracking is never achieved at $\hat{\rho} = 0.15, 0.3$. In fact, a steady-state error can be observed after 2.5 s at these two control points. On the other hand, the figure indicates that the controller is able to track the target without any steady-state error in the second test case, thus demonstrating the benefits of incorporating moving sources in certain scenarios. Fig. 2 also shows that the entire safety-factor profile at $t = 4$ s. A significant difference in the safety-factor profile between the two test cases can be observed in the core. In the first case, the safety-factor profile at $t = 4$ s is monotonically increasing. On the other hand, the safety-factor profile in the second case has a reversed magnetic shear shape that is much closer to the target.

The input trajectories generated by the controller in the first and second cases, shown in Figs. 3 and 4, respectively, indicate the potential reasons for the difference in the controller performance. For instance, as shown in Fig. 3, the controller almost completely saturates the current drives when the controller is active in the first case. Thus, the upper and lower bounds on the actuators' powers prevent the controller from attaining the safety-factor target values shown in Fig. 2 when the EC H&CD deposition locations are fixed. On the contrary, such extensive saturation of all the current drives does not occur when the controller determines the EC H&CD deposition locations in real-time (Fig. 4). The two figures also indicate that the plasma current in both cases follows a similar trajectory. Additionally, in both cases, a spike in the NBI and EC H&CD powers can be observed immediately after

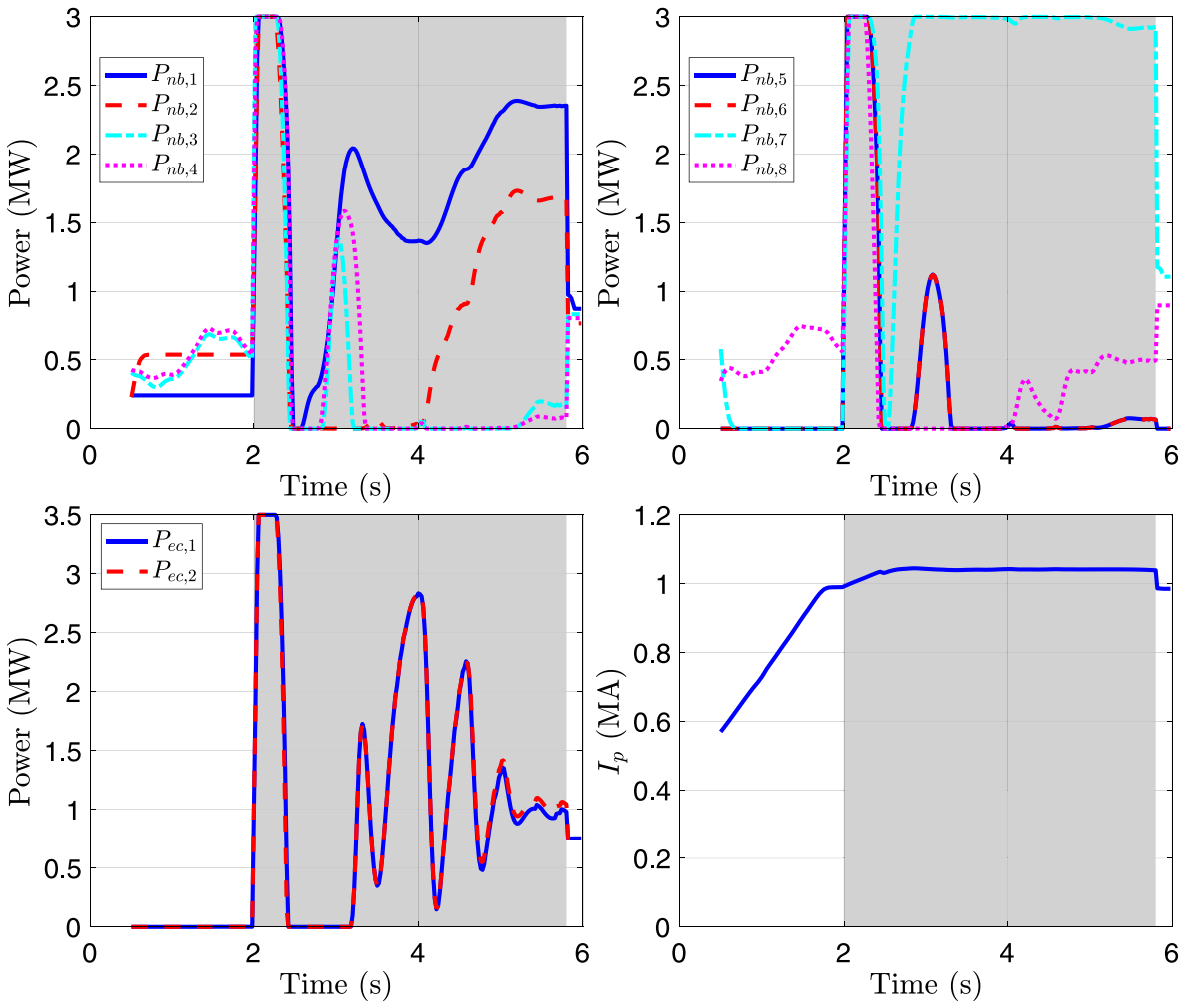

Fig. 4. Inputs of moving EC H&CD deposition locations case — top right: $P_{nb,i}, i \in \{1,2,3,4\}$, top left: $P_{nb,i}, i \in \{5,6,7,8\}$, bottom right: $P_{ec,i}, i \in \{1,2\}$, bottom left: I_p.

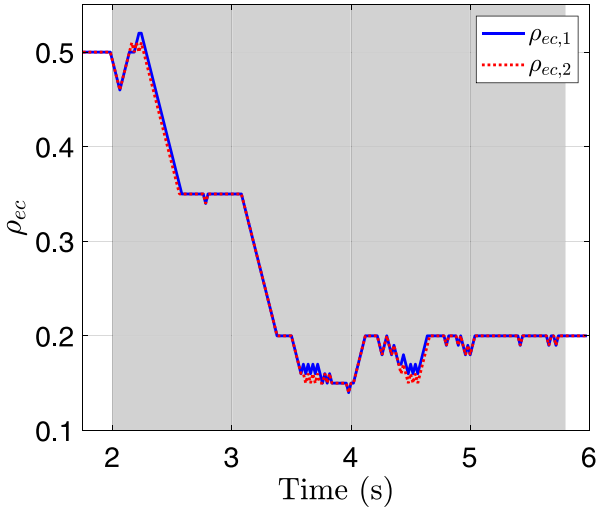

Fig. 5. The EC H&CD deposition locations ($\rho_{ec,1}$, $\rho_{ec,2}$) determined by the controller in the second case.

controller activation. This sudden increase in power is because the error between the target and actual states at the interior control points ($\hat{\rho} = 0.15, 0.3$) is maximum at the instance of controller activation, and the controller is saturating the inputs to attain the target. However, once the target is reached in the second case, the controller is able to modulate the auxiliary drive powers to maintain the target. On the other hand, the target is never achieved in the first case, as emphasized earlier.

Fig. 5 illustrates the EC H&CD deposition locations determined by the controller in the second case. Once the controller is activated, the EC H&CD deposition locations are adapted to achieve the desired safety-factor target. For this particular scenario, the deposition locations of both the EC H&CDs $\rho_{ec,1}$ and $\rho_{ec,2}$ follow a similar trajectory. Another important aspect to note here is that the inputs shown in Fig. 4 are smooth without high-frequency chatter even when the EC H&CD deposition locations shown in Fig. 5 are varying.

5. Conclusion

This work presents an MPC-based algorithm for safety-factor control that prescribes the auxiliary drive powers, plasma current, and EC H&CD deposition locations simultaneously. A control-oriented linear model that incorporates EC H&CD deposition location dynamics is derived. Then, the MPC problem is formulated for the case when the EC deposition locations are fixed. An iterative algorithm is then wrapped around the traditional (fixed deposition location) MPC algorithm to determine the optimal EC H&CD deposition locations. Simulations based on response models more complex than those used for control synthesis illustrate that the control algorithm is able to robustly achieve the desired target while simultaneously allocating auxiliary drive powers, plasma current, and the EC H&CD deposition locations.

Furthermore, the input trajectories are smooth even when the EC H&CD deposition locations are varied. Future work can involve incorporating more sophisticated models for EC H&CD dynamics, optimizing the proposed algorithm for computational efficiency using parallel computing techniques, and exploring other MPC techniques for simultaneous optimization of both the current drive powers and EC positions.

Declaration of competing interest

The authors declare that they have no known competing financial interests or personal relationships that could have appeared to influence the work reported in this paper.

Data availability

The authors do not have permission to share data.

Acknowledgments

This material is based upon work supported by the U.S. Department of Energy, Office of Science, Office of Fusion Energy Sciences, under Award Number DE-SC0010661.

References

[1] M. Boyer, et al., Central safety factor and β_N control on NSTX-U via beam power and plasma boundary shape modification, using TRANSP for closed loop simulations, Nucl. Fusion 55 (5) (2015) 053033, http://dx.doi.org/10.1088/0029-5515/55/5/053033.

[2] M.D. Boyer, et al., First-principles-driven model-based current profile control for the DIII-D tokamak via LQI optimal control, Plasma Phys. Control. Fusion 55 (10) (2013) 105007, http://dx.doi.org/10.1088/0741-3335/55/10/105007.

[3] C. Xu, et al., Sequential linear quadratic control of bilinear parabolic PDEs based on POD model reduction, Automatica 47 (2) (2011) 418–426, http://dx.doi.org/10.1016/j.automatica.2010.11.001.

[4] W. Wehner, et al., Optimal current profile control for enhanced repeatability of L-mode and H-mode discharges in DIII-D, Fusion Eng. Des. 123 (2017) 513–517, http://dx.doi.org/10.1016/j.fusengdes.2017.03.022.

[5] Y. Ou, et al., Receding-horizon optimal control of the current profile evolution during the ramp-up phase of a tokamak discharge, Control Eng. Pract. 19 (1) (2011) 22–31, http://dx.doi.org/10.1016/j.conengprac.2010.08.006.

[6] E. Maljaars, et al., Control of the tokamak safety factor profile with time-varying constraints using MPC, Nucl. Fusion 55 (2) (2015) 023001, http://dx.doi.org/10.1088/0029-5515/55/2/023001.

[7] E. Maljaars, et al., Profile control simulations and experiments on TCV: A controller test environment and results using a model-based predictive controller, Nucl. Fusion 57 (12) (2017) 126063, http://dx.doi.org/10.1088/1741-4326/aa8c48.

[8] J.E. Barton, et al., Physics-based control-oriented modeling and robust feedback control of the plasma safety factor profile and stored energy dynamics in ITER, Plasma Phys. Control. Fusion 57 (11) (2015) 115003, http://dx.doi.org/10.1088/0741-3335/57/11/115003.

[9] F.B. Argomedo, et al., Lyapunov-based distributed control of the safety-factor profile in a tokamak plasma, Nucl. Fusion 53 (3) (2013) http://dx.doi.org/10.1088/0029-5515/53/3/033005.

[10] F.B. Argomedo, et al., A strict control Lyapunov function for a diffusion equation with time-varying distributed coefficients, IEEE Trans. Automat. Control 58 (2) (2013) 290–303, http://dx.doi.org/10.1109/TAC.2012.2209260.

[11] B. Mavkov, et al., Experimental validation of a Lyapunov-based controller for the plasma safety factor and plasma pressure in the TCV tokamak, Nucl. Fusion 58 (5) (2018) 056011, http://dx.doi.org/10.1088/1741-4326/aab16a.

[12] N.T. Vu, et al., Plasma internal profile control using IDA-PBC: Application to TCV, Fusion Eng. Des. 123 (2017) 624–627, http://dx.doi.org/10.1016/j.fusengdes.2017.02.074.

[13] M.D. Boyer, et al., Backstepping control of the Toroidal plasma current profile in the DIII-D Tokamak, IEEE Trans. Control Syst. Technol. 22 (5) (2014) 1725–1739, http://dx.doi.org/10.1109/TCST.2013.2296493.

[14] J. Barton, et al., Physics-model-based nonlinear actuator trajectory optimization and safety factor profile feedback control for advanced scenario development in DIII-D, Nucl. Fusion 55 (9) (2015) http://dx.doi.org/10.1088/0029-5515/55/9/093005.

[15] A. Pajares, E. Schuster, Safety factor profile control in tokamaks via feedback linearization, in: 55th IEEE Conference on Decision and Control, CDC, 2016, pp. 5668–5673, http://dx.doi.org/10.1109/CDC.2016.7799140.

[16] A. Pajares, E. Schuster, Current profile and normalized beta control via feedback linearization and Lyapunov techniques, Nucl. Fusion (2021) 21.

[17] S.T. Paruchuri, A. Pajares, E. Schuster, Minimum safety factor control in tokamaks via optimal allocation of spatially moving electron cyclotron current drive, in: 60th IEEE Conference on Decision and Control, CDC, 2021, pp. 454–459, http://dx.doi.org/10.1109/CDC45484.2021.9683130.

[18] F.L. Hinton, R.D. Hazeltine, Theory of plasma transport in toroidal confinement systems, Rev. Modern Phys. 48 (2) (1976) 239–308, http://dx.doi.org/10.1103/RevModPhys.48.239, URL https://link.aps.org/doi/10.1103/RevModPhys.48.239.

[19] J.E. Barton, et al., Physics-based control-oriented modeling of the safety factor profile dynamics in high performance tokamak plasmas, in: 52nd IEEE Conference on Decision and Control, 2013, pp. 4182–4187, http://dx.doi.org/10.1109/CDC.2013.6760531.

[20] A. Pajares, E. Schuster, Integrated control and actuator management strategies for internal inductance and normalized beta regulation, Fusion Eng. Des. 170 (2021) 112526, http://dx.doi.org/10.1016/j.fusengdes.2021.112526.

[21] H. Wang, Model-based Control of the Current Density Profile in the Experimental Advanced Superconducting Tokamak (EAST) (Ph.D. thesis), Lehigh University, 2019.

[22] G. Pannocchia, et al., Offset-free MPC explained: Novelties, subtleties, and applications, IFAC-PapersOnLine 48 (23) (2015) 342–351.

[23] J. Nocedal, S.J. Wright, Numerical Optimization, Springer, 1999.

[24] A. Pajares, Integrated Control in Tokamaks using Nonlinear Robust Techniques and Actuator Sharing Strategies (Ph.D. thesis), Lehigh University, Bethlehem, PA, USA, 2019.